



Cite this: DOI: 10.1039/c7ta07183c

## Microgel-assisted assembly of hierarchical porous reduced graphene oxide for high-performance lithium-ion battery anodes†

Huan Wang,<sup>a</sup> Jingyi Xie,<sup>a</sup> Haider Almkhelfe,<sup>a</sup> Victoria Zane,<sup>a</sup> Raiya Ebini,<sup>b</sup> Christopher M. Sorensen<sup>b</sup> and Placidus B. Amama  \*<sup>a</sup>

Graphene has emerged as one of the foremost candidates for replacing graphite anodes in lithium-ion batteries (LIBs) due to its unique physical and electrochemical properties. Most techniques for synthesis of graphene-based electrode materials utilize graphene oxide (GO). However, restacking of GO sheets during common fabrication processes usually results in significant loss of usable Li-insertion sites, and consequently, a substantial decrease in cycling performance of the electrode. In this work, we demonstrate a facile and scalable approach for fabrication of 3D, hierarchical macro/mesoporous reduced graphene oxide (RGO) anodes for LIBs using a polymer sphere (PS) microgel as a template. The synthesis process involves controlled encapsulation of GO sheets on the surface of thermal degradable PS microgels, followed by shrinkage of PS microgels to generate GO wrinkles. The GO-wrapped cross-linked PS swells to a microgel in *N*-methyl-2-pyrrolidone (NMP), while it shrinks after replacing the NMP with distilled water. The overall specific surface area of the resulting porous/wrinkled RGO with mesopores and macropores, obtained by annealing the wrinkled GO@shrunken PS, increases from  $96\text{ m}^2\text{ g}^{-1}$  to  $276\text{ m}^2\text{ g}^{-1}$ ; the highly porous structure also shortens the transport length of Li ions. The porous/wrinkled RGO anode material achieves a high reversible capacity and durability ( $\sim 720\text{ mA h g}^{-1}$  at 0.2C after 200 cycles), and a high rate capability ( $\sim 160\text{ mA h g}^{-1}$  at 20C). The electrode performance is comparable to the best RGO anodes. The microgel-assisted method opens up a promising route for potentially controlling the properties of 3D graphene-based electrodes.

Received 14th August 2017  
Accepted 18th October 2017

DOI: 10.1039/c7ta07183c  
[rsc.li/materials-a](http://rsc.li/materials-a)

## 1. Introduction

Lithium-ion batteries (LIBs) are modern energy storage devices that have shown substantial promise in solving the global demand for energy.<sup>1,2</sup> Recent efforts have focused on improving performance of LIBs, with respect to their energy and power densities, cyclability, and safety. Electrode performance in LIBs is dependent on choice of electrode material and its inner architecture.<sup>3,4</sup> Among possible electrode materials, graphene has emerged as one of the foremost candidates due to its unique material properties, including excellent electrical conductivity ( $2000\text{ S cm}^{-1}$ ) that far exceeds that of graphitic carbon, high chemical tolerance, and large theoretical specific surface area ( $2630\text{ m}^2\text{ g}^{-1}$ ), as well as a broad electrochemical window between 0.01 and 3.5 V.<sup>2,5,6</sup>

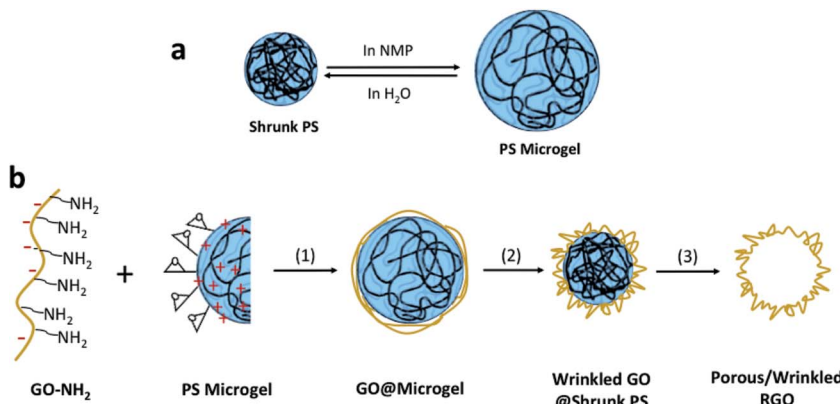
A scalable and cost-effective approach for fabricating graphene-based electrode materials involves use of graphene oxide (GO) obtained *via* direct exfoliation of graphite. However,

due to van der Waals interactions and the high aspect ratio of GO sheets, the sheets can easily restack and form a bulk graphite-like structure during conventional synthesis processes.<sup>7</sup> The restacking of graphene sheets results in significant loss of usable Li-insertion sites, and consequently, a decrease in specific capacity and rate capability of the electrode.<sup>5</sup> Therefore, it is necessary to develop synthesis strategies that preserve the interlayer space and Li insertion sites of graphene. A number of studies have been conducted on the assembly of graphene sheets into three-dimensional (3D) graphene networks with controlled morphology for accommodating the ubiquitous restacking of graphene sheets.<sup>8–10</sup> Recent reports have shown that graphene with micro/meso/macropores can reduce the Li-ion diffusion distance and provide additional Li ion storage sites due to the ultra-thin shells and available active edges of pores.<sup>8,11</sup> Conventional approaches for design of porous graphene structures have taken advantage of sacrificial templates such as inorganic oxides and colloidal particles.<sup>9,12,13</sup> Besides template-assisted designs, self-assembly strategies (*e.g.*, spray-assisted deep-frying process<sup>10</sup> and “breath figure” method<sup>14</sup>) have also been used to fabricate 3D graphene structures with high surface areas and porosity that support fast Li-ion diffusion. However, controlled synthesis of 3D

<sup>a</sup>Department of Chemical Engineering, Kansas State University, Manhattan, KS 66506, USA. E-mail: [pamana@ksu.edu](mailto:pamana@ksu.edu); Fax: +1-785-532-7372

<sup>b</sup>Department of Physics, Kansas State University, Manhattan, KS 66506, USA

† Electronic supplementary information (ESI) available. See DOI: [10.1039/c7ta07183c](https://doi.org/10.1039/c7ta07183c)



**Scheme 1** (a) Schematic illustration of swelling and shrinking process of cross-linked PS in NMP and distilled water, respectively. (b) Schematic illustration of the synthesis of a porous/wrinkled RGO structure: (1) ring-opening reaction and charge attraction between GO-NH<sub>2</sub> and PS microgel in NMP; (2) shrinking of GO@microgel to wrinkled GO@shrunken PS in water; (3) removal of PS by annealing treatment at 600 °C for 3 hours.

hierarchical graphene structures with mesopores and macropores as well as unstacked graphene sheets, remains a challenge.

Motivated by strategies discussed above, we demonstrate the synthesis of 3D, hierarchical, porous/wrinkled reduced graphene oxide (RGO) anodes *via* a microgel-assisted method. The facile and scalable approach (Scheme 1) involves controlled wrapping of GO sheets on the surface of thermal, degradable polymer sphere (PS) microgels, followed by shrinkage of PS microgels to generate GO wrinkles. To the best of our knowledge, this is the first study that utilizes controlled swelling of PS microgels in an organic solvent and subsequent shrinking in water to produce 3D hierarchical macro/mesoporous RGO. The formed porous/wrinkled RGO, with macropores (diameter ~200 nm) and large amounts of mesopores (diameter ~3.9 nm) in the gap of neighboring RGO wrinkles after removal of PS, not only effectively reduces the Li-ion diffusion resistance inside RGO sheets, but also provides additional accessible sites (on the walls and edges of pores) for Li-ion intercalation. The resulting anode material achieves a high reversible capacity (~720 mA h g<sup>-1</sup> at 0.2C) and high rate capability (~160 mA h g<sup>-1</sup> at 20C). Moreover, the microgel-assisted approach described in this study opens up a promising strategy for controlled fabrication of 3D graphene-based electrodes.

## 2. Experimental section

### 2.1. Synthesis of GO-NH<sub>2</sub>/NMP dispersion

GO was synthesized from natural flake graphite by the modified Hummers method.<sup>15</sup> A solution of 1 mg mL<sup>-1</sup> GO-NH<sub>2</sub> and *N*-methyl-2-pyrrolidone (NMP) was prepared by mixing and stirring an initial mixture of 40 mg of GO and 4 mL 28% ammonium hydroxide solution with 40 mL of NMP solvent at 60 °C for 9 hours.

### 2.2. Synthesis of cross-linked poly(methyl methacrylate-*co*-glycidyl methacrylate-*co*-butyl acrylate) [P(MMA-GMA-BA)] polymer spheres

Four g methyl methacrylate (MMA), 0.8 g glycidyl methacrylate (GMA), 0.2 g butyl acrylate (BA), and 5 µL divinylbenzene (DVB)

were first emulsified by 0.08 g 2,2'-azobis(2-methylpropionamide) dihydrochloride (AIBA) in a 100 mL round-bottom flask with 50 mL of distilled water. The solution was then flushed with nitrogen for 30 min to remove oxygen. The polymerization reaction was carried out for 3 hours in a nitrogen atmosphere at a fixed temperature of 65 °C, while being stirred at 550 rpm. Resulting milky dispersions were filtered and purified by repeated washing with ethanol and distilled water. Finally, cross-linked P(MMA-GMA-BA) polymer spheres were dried in a vacuum oven at 50 °C for 24 hours.

### 2.3. Synthesis of 3D hierarchical porous/wrinkled RGO anodes

A 0.02 g mL<sup>-1</sup> PS microgel/NMP dispersion was prepared by swelling as-synthesized P(MMA-GMA-BA) polymer spheres in NMP solvent at room temperature. Forty mL of 1 mg mL<sup>-1</sup> GO-NH<sub>2</sub>/NMP dispersion was used to wrap 4 mL of the 0.02 g mL<sup>-1</sup> PS microgel/NMP dispersion. The wrapping process was then carried out at 60 °C for 8 hours. After wrapping the microgel with GO sheets, the as-synthesized solution was added dropwise to distilled water, resulting in a volumetric ratio of 1 : 7 for as-synthesized solution and distilled water, respectively; this step was carried out to shrink the volume of GO-encapsulated microgels (GO@microgels) and form wrinkled GO-encapsulated shrunk PS (wrinkled GO@shrunken PS). Porous/wrinkled RGO was obtained by annealing the wrinkled GO@shrunken PS under argon at 600 °C for 3 hours. Final steps for preparing the anode material involved mixing the porous/wrinkled RGO and poly(vinylidene difluoride) (PVDF) binder at a mass ratio of 9 : 1, respectively. The mixture was then sonicated in NMP and dip-coated onto a copper current collector (9 µm thick) to form a dry layer under vacuum at 100 °C with an estimated mass loading of ~1 mg cm<sup>-2</sup>.

### 2.4. Structural and chemical characterization

The morphological characterization of the samples was conducted using a field emission scanning electron microscope

(FESEM, Hitachi S5200) and a transmission electron microscope (TEM, FEI Tecnai F20 XT). For TEM imaging, a small amount of wrinkled GO@shrunk PS sample was dispersed in water *via* ultrasonication; a drop of the homogeneous suspension was deposited on a holey carbon TEM grid and examined by TEM operating at 200 kV. X-ray photoelectron spectroscopy (XPS) data were obtained using a PerkinElmer PHI 5400 electron spectrometer with an achromatic Al K $\alpha$  X-ray source (1486.6 eV) operating at 300 W (15 kV and 20 mA). Base pressure of the chamber during measurement was controlled at less than  $5 \times 10^{-8}$  Torr. Before testing the samples, the spectrometer was calibrated by setting the binding energies of Au 4f<sub>7/2</sub> and Cu 2p<sub>3/2</sub> to 84.0 and 932.7 eV, respectively. The analyzer pass energy was set to 44.8 eV and contact time was 100 ms. For high-resolution measurement of O 1s, N 1s, and C 1s spectra, the analyzer's pass energy was set to 17.9 eV and contact time was 25 ms. All XPS spectra were charge-corrected by referencing to C 1s peak at 284.6 eV. Thermogravimetric analysis (TGA) was performed on a TGA-550 analyzer (TA Instruments) under a stream of N<sub>2</sub> flow (100 sccm) with a temperature ramp of 5 °C min<sup>-1</sup> from room temperature to 600 °C. FTIR spectra were recorded on a Cary 630 Agilent spectrometer at a resolution of 4 cm<sup>-1</sup>. Raman spectra were obtained using an iHR550 spectrometer at a wavelength of 532 nm. Dynamic light scattering (DLS) was performed at a scattering angle of 90° using a 35 mW He–Ne laser and a Langley-Ford correlator. P(MMA–GMA–BA)/NMP dispersion was diluted by NMP and sonicated for 1 hour before DLS measurement.

### 2.5. Electrochemical measurements

Assembly of the half-cell took place in an argon-filled glovebox with concentrations of moisture and oxygen below 0.5 ppm. A standard sized coin cell (diameter of ~18 mm and height of ~4 mm) was used for electrochemical testing. The working electrode was produced by coating the mixture of porous/wrinkled RGO and PVDF (10 wt%) binder on a Cu foil current collector. Microporous polypropylene membrane and Li foil were used as the separator and counter electrode, respectively. The electrolyte used was 1 M LiPF<sub>6</sub> solution in an ethylene carbonate (EC)/dimethyl carbonate (DMC)/diethyl carbonate (DEC) mixture (1 : 1 : 1, in vol%). On a Maccor 4300 electrochemical workstation, cyclic voltammetry (CV) of the cells was performed at 0.1 mV s<sup>-1</sup> in the voltage range of 0.002–3.000 V, while galvanostatic cycling experiments were tested in the voltage range of 0.002–3.000 V *versus* Li<sup>+</sup>/Li at room temperature.

## 3. Results and discussion

### 3.1. Fabrication of porous/wrinkled RGO anode

Scheme 1 illustrates the overall synthetic procedure of hierarchical macro/mesoporous RGO materials. As shown in Scheme 1a, cross-linked PS swells to microgel in NMP; however, microgel shrinks back to shrunk PS after replacing NMP with distilled water. Solubility of the polymer in solvents plays an important role in formation and shrinking of microgels. In a “good solvent,” the polymer chains will adopt a self-avoiding

random walk configuration that maximizes contact with the solvent. However, in a “poor solvent,” the polymer chains collapse, forming a dense polymer mass that excludes solvent molecules from their interior. To satisfy the lower free energy at a given temperature, the polymer chains adopt a crumpled spherical state. Scheme 1b shows the three main synthetic steps for porous/wrinkled RGO anodes. In step (1), PS microgels are encapsulated with a thin layer of smooth GO sheets, possibly due to two reasons. First, the epoxy groups on the surface of PS microgels may undergo ring-opening reaction with NH<sub>2</sub> groups on the surface of GO. Second, electrostatic attraction exists between oxygen functionalities on GO and positive charges on the surface of PS microgels. In step (2), the PS microgels shrink to significantly smaller sizes, due to the precipitation of PS in water, which is accompanied by crumpling of the smooth GO sheets. Consequently, wrinkling of GO sheets perpendicular to the shrunk gel surface are forced to form during shrinkage in water, and large amounts of mesopores are created in the gap of neighboring GO wrinkles. Finally, the PS templates are removed by an annealing treatment to produce 3D, hierarchical, macro/mesoporous RGO materials. While use of PS microgels for templated synthesis is not new, to the best of our knowledge, this is the first study that utilizes different solvents to swell and shrink PS microgels wrapped with GO sheets to fabricate macro/mesoporous RGO materials. In principle, 3D properties of the macro/mesoporous RGO materials can be tuned by changing the properties of PS microgels.

### 3.2. Characterization of P(MMA–GMA–BA), GO, and GO–NH<sub>2</sub>

The IR spectrum of as-synthesized P(MMA–GMA–BA) is shown in Fig. 1. All characteristic IR bands corresponding to poly(methyl methacrylate) (PMMA) segments are identified using data in the literature.<sup>16,17</sup> Because GMA and BA have similar molecular structures to MMA, most of the characteristic peaks for poly(glycidyl methacrylate) (PGMA) and poly(butyl acrylate) (PBA) segments overlap with the spectrum of PMMA segments.<sup>18,19</sup> The two bands at 2997 cm<sup>-1</sup> and 2952 cm<sup>-1</sup> are attributed to the C–H bond stretching vibrations of –CH<sub>3</sub> and –CH<sub>2</sub> groups, respectively. The strong band at 1730 cm<sup>-1</sup> shows the presence of the acrylate carboxylic group. Absorption bands from 1395 cm<sup>-1</sup> to 1450 cm<sup>-1</sup> originate from –CH<sub>3</sub> and –CH<sub>2</sub>

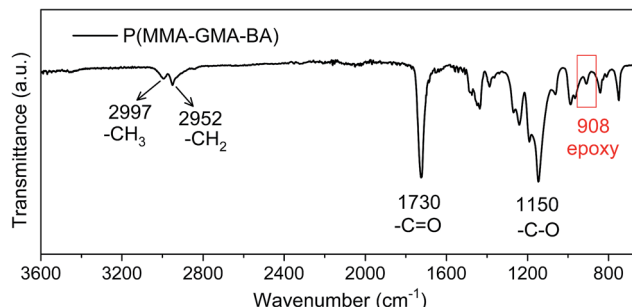


Fig. 1 FT-IR spectrum of as-synthesized P(MMA–GMA–BA) spheres (0.1 wt% DVB).

deformation vibration, while at  $1150\text{ cm}^{-1}$ , C–O–C stretching vibration can be observed. The distinct absorption peak at  $908\text{ cm}^{-1}$  is attributed to the epoxy group stretching of PGMA,<sup>18</sup> confirming successful copolymerization of PGMA. The epoxy groups introduced on the surface of P(MMA–GMA–BA) spheres are capable of linking with the NH<sub>2</sub> groups on GO sheets via ring-opening reaction.

Incorporation of amino groups onto the GO surface was probed by XPS. Fig. 2 shows XPS survey and high-resolution C 1s and N 1s scans of GO and GO-NH<sub>2</sub>. A distinct signal of N is observed only at a binding energy of 400 eV in the survey scan of GO-NH<sub>2</sub> (Fig. 2a). C 1s XPS spectra show a significant decrease in the C–O bond peak at approximately 286.7 eV after the amination reaction (Fig. 2b), due to the reduction in the content of oxygen-containing functional groups on GO.<sup>20</sup> The N 1s spectrum (Fig. 2c) is characterized by a broad peak located at a binding energy of  $\sim 400$  eV, which is related to the two different nitrogen functionalities including NH<sub>4</sub><sup>+</sup> and NH<sub>2</sub> bonded to GO.<sup>21</sup> In addition, the Raman spectra of GO and GO-NH<sub>2</sub> in Fig. 2d show an increase in the intensity ratio of D- and G-bands ( $I_D/I_G$ ); the  $I_D/I_G$  increases from 0.81 for GO to 0.99 for GO-NH<sub>2</sub>, most likely indicate the creation of more defect sites due to intercalation of N atoms in the carbon structure of GO.<sup>22</sup> Further comparison of the Raman spectral features reveals the G-band for GO at  $1593\text{ cm}^{-1}$  is shifted to  $1600\text{ cm}^{-1}$  for GO-NH<sub>2</sub>, a phenomenon attributed to the successful amination of GO.<sup>23,24</sup>

To confirm the existence of GO-NH<sub>2</sub> bond, XPS spectra were collected for GO-NH<sub>2</sub> after ion exchange treatment for three

days with HCl (pH = 1) to replace NH<sub>4</sub><sup>+</sup> with H<sup>+</sup>. The GO-NH<sub>2</sub>/HCl aqueous solution was repeatedly washed and centrifuged with distilled water until HCl was completely removed and GO-NH<sub>2</sub> sheets could form a highly stable dispersion in water. We emphasize the XPS survey scan of GO-NH<sub>2</sub> still showed a distinct N 1s peak after completely removing NH<sub>4</sub><sup>+</sup>. Since the reaction between ammonia solution and GO was performed under low temperature ( $\sim 60\text{ }^\circ\text{C}$ ), it is highly unlikely that the doping of N in the carbon-skeleton ring of GO occurred. As shown in Fig. S1† the N 1s spectrum can be fitted with two components: first peak component at 399.6 eV that is attributed to C–NH<sub>2</sub> and produced by ring open reaction between epoxy group of GO and ammonia solution, and the second peak at 401.9 eV that is assigned to NH<sub>4</sub><sup>+</sup> and ionically bonded to COO<sup>-</sup> group. As Fig. S1† shows, the peak intensity of the component associated with NH<sub>4</sub><sup>+</sup> decreases substantially after ion exchange; however, the peak intensity of NH<sub>2</sub> remains almost the same. We therefore conclude that the N in our synthesized GO-NH<sub>2</sub> is in fact covalently bonded to C, as opposed to having ionic bonds between NH<sub>4</sub><sup>+</sup> and COO<sup>-</sup> species. The N content calculated from XPS data is  $\sim 4.5$  at%, which is expected to provide additional electrochemically active sites on the surface of GO and further increase the Li storage capacity of porous/wrinkled RGO after annealing treatment.<sup>25</sup>

### 3.3. Characterization of microstructure

PS synthesized with 0, 0.1, and 0.5 wt% DVB, and their corresponding PS/NMP dispersions are labeled as samples A1, A2, and A3 in Fig. 3a, respectively. DVB is an active bifunctional

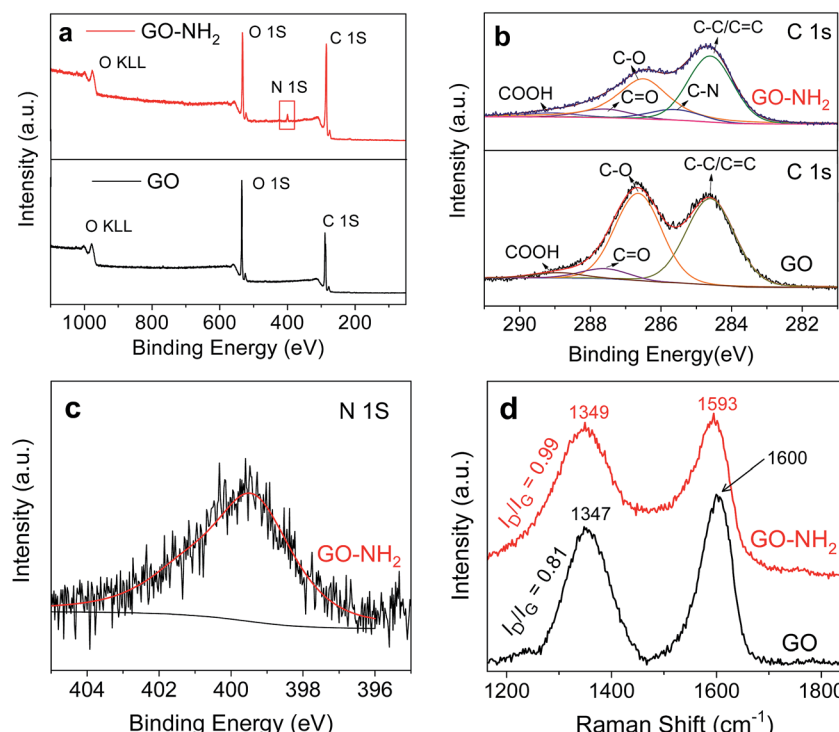


Fig. 2 (a) XPS survey spectra of GO-NH<sub>2</sub> and GO; (b) C 1s XPS spectra of GO-NH<sub>2</sub> and GO; (c) N 1s XPS spectrum of GO-NH<sub>2</sub>; and (d) Raman spectra of GO and GO-NH<sub>2</sub>.

monomer with two C=C double bonds in one molecule, which can link linear polymer chains to form a 3D network structure. The molecular structure of as-synthesized cross-linked PS is presented in Scheme S1.<sup>†</sup> As shown in Fig. 3a, uncross-linked PS will dissolve in NMP to form transparent homogenous P(MMA-GMA-BA) solution. In the case of slightly cross-linked PS (0.1% DVB), a translucent dispersion of microgel is observed. The difference in refractive index between microgel and solvent decreases, because a large quantity of solvent molecules are absorbed into the microgel, which may cause the opaque solution of PS to become translucent. For highly cross-linked PS (0.5% DVB), the higher cross-link density limited the swelling of

the microgel with less solvent absorbed into it, and as a consequence, the PS (0.5% DVB) microgel remained opaque.

Average size of the PS microgel (0.1 wt% DVB) was evaluated using DLS (Fig. 3b). Nanoparticles in suspension undergo random thermal motion (Brownian motion). The hydrodynamic size of particles was determined by the Stokes–Einstein equation (eqn (1)) where  $D_h$  is the hydrodynamic diameter (or particle size),  $D_t$  is the translational diffusion coefficient,  $k_B$  is Boltzmann's constant,  $T$  is thermodynamic temperature, and  $\eta$  is dynamic viscosity.

$$D_h = \frac{k_B T}{3\pi\eta D_t} \quad (1)$$

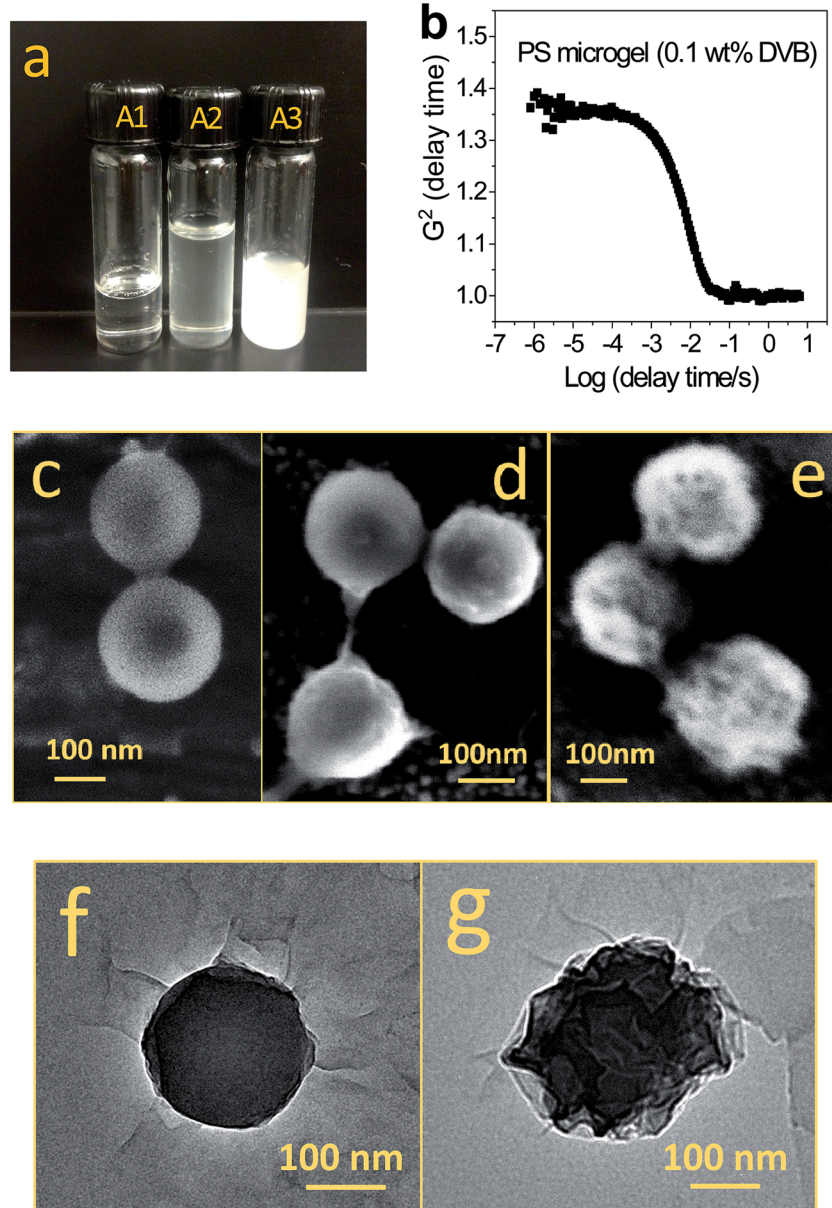


Fig. 3 (a) Picture of PS/NMP dispersions ( $0.02 \text{ g mL}^{-1}$ ) for PS synthesized with 0, 0.1, and 0.5 wt% DVB shown as sample A1, A2, and A3, respectively. (b) Correlation function  $G^2(t)$  of the diluted PS/NMP dispersion at  $25^\circ\text{C}$  measured by DLS. (c) SEM image of as-synthesized PS (0.1 wt% DVB); (d) and (f) SEM and TEM images of GO wrapped as-synthesized PS (0.1 wt% DVB) with smooth GO surfaces, respectively; and (e) and (g) SEM and TEM images of wrinkled GO@shrunken PS with wrinkled GO surfaces, respectively.

The average hydrodynamic diameter of the microgel is 623 nm while that of as-synthesized PS (0.1 wt% DVB) is 256 nm (Fig. S2†). Diameters obtained by DLS are usually larger than those observed in SEM or TEM images, because DLS measures the hydrodynamic radius of particles in the large-size end of the size distribution in the laser beam path; and the solvent molecules may be clustered around the particle, forming a solvation shell around the sphere. SEM images of GO-NH<sub>2</sub> are shown in Fig. S3.† The size of GO-NH<sub>2</sub> is around 0.2–1.2 μm, which matches well with that of the PS microgel with a size of 623 nm, and can thus facilitate the assembly of GO on the surface of a microgel. Fig. 3c and S4† show representative SEM images of the highly uniform, uncoated as-synthesized PS (0.1 wt% DVB) with smooth textures and an average diameter of 220 nm; additional images used for obtaining average diameter are presented in Fig. S5.† SEM and TEM images reveal the difference in the surface properties of GO-wrapped as-synthesized PS (Fig. 3d and f) and wrinkled GO@shrunk PS (Fig. 3e and g). Fig. 3d and f indicate the surface of the as-synthesized PS was coated by relatively smooth untextured GO sheets. In contrast, Fig. 3e and g show more wrinkled and roughened textures associated with the shrinking of GO sheets and are encapsulating the PS microgel in water. Furthermore, from TEM images (Fig. S6 and S7†), thicknesses of GO layers wrapping on as-synthesized PS and shrunk PS fall in the range of 5–12 nm and 42–80 nm, respectively. Such differences indicate the successful formation of GO wrinkles for wrinkled GO@shrunk

PS. In particular, the wrinkled GO sheets generate numerous mesopores between the neighboring wrinkles that enhance the surface area.

As revealed by the SEM images (Fig. 4a and b), wrinkled/porous RGO electrodes are characterized by deflated hollow-pore structures with intact and continuous walls after annealing treatment. Thermal stability of the core PS was analyzed by TGA (Fig. S8†) and results reveal that PS starts to degrade at 280 °C and fully decomposes at 430 °C, after ~2.5 hours of annealing in N<sub>2</sub> flow. Average size of the deflated pore structures is approximately 200 nm, which can provide a suitable contact area with electrolytes and ions. For purpose of comparison, the paper-like stacked RGO material is presented in Fig. 4c. No obvious macropores (diameter > 50 nm) are observed in the stacked RGO sheets.

The structural difference was further confirmed by nitrogen adsorption/desorption data of porous/wrinkled RGO and stacked RGO (Fig. 4d). Although the specific surface area of porous/wrinkled RGO is smaller ( $276 \text{ m}^2 \text{ g}^{-1}$ ) than that of single-layer graphene sheets ( $2630 \text{ m}^2 \text{ g}^{-1}$ ),<sup>6</sup> it is still larger than that of stacked RGO ( $96 \text{ m}^2 \text{ g}^{-1}$ ). Note that since electrodes with high surface areas normally induce high irreversible capacities during the first charge/discharge cycle, optimum surface area for a high-performance electrode may be far less than the theoretical surface area of graphene. The porous/wrinkled RGO presents a characteristic type IV isotherm according to the IUPAC classification, with a pronounced hysteresis at  $P/P_0 = 0.45\text{--}0.96$ ,

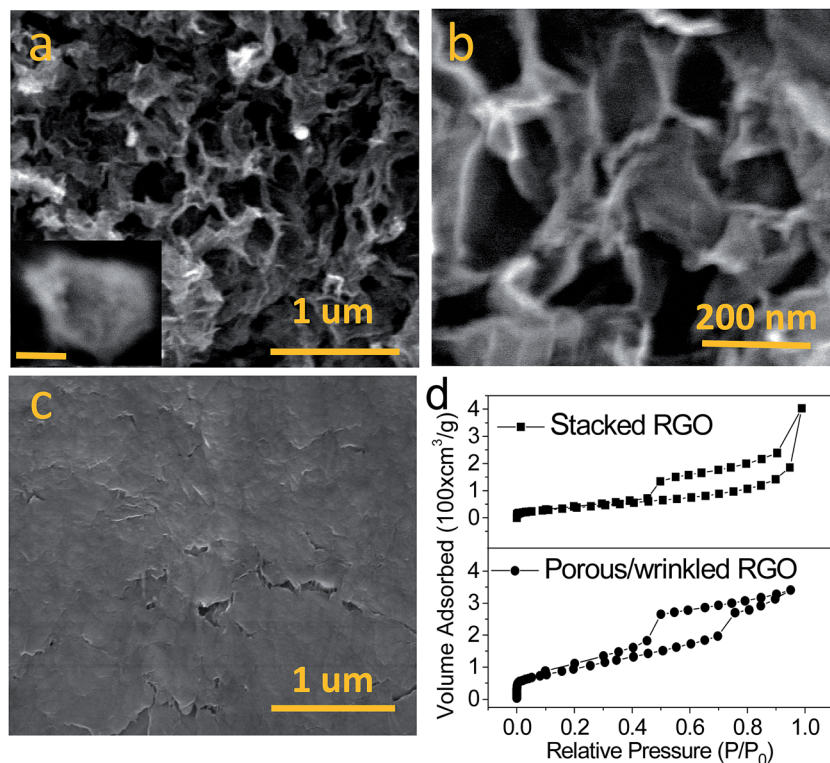


Fig. 4 (a) Low-magnification SEM image of porous/wrinkled RGO after annealing treatment; the inset shows an image of wrinkled GO@shrunk PS before annealing treatment (scale bar = 150 nm). (b) High-magnification SEM image of porous/wrinkled RGO after annealing treatment. (c) Low-magnification SEM image of stacked RGO sheets. (d) Nitrogen adsorption–desorption isotherms of porous/wrinkled RGO and stacked RGO.

suggesting the existence of high number of mesopores (2–50 nm) in porous/wrinkled RGO sample.<sup>26</sup> Additionally, the hysteresis suggests the occurrence of irreversible chemical adsorption in the mesopores,<sup>27</sup> which is usually associated with capillary condensation in the pores. The average pore diameter of porous/wrinkled RGO is roughly 3.9 nm calculated by the BJH (Barrett–Joyner–Halenda) method (Fig. S9†). A number of studies have questioned the accuracy of pore size distributions (PSDs) in the nanometer range obtained from the BJH method that is based on classical thermodynamic methods.<sup>28–30</sup> To address this drawback of the BJH method, we have also used nonlocal density functional theory (NLDFT) for analysis of pore structure of stacked and wrinkled RGO. NLDFT is designed for adsorption and capillary condensation in capillary pores and provides a more accurate estimation of the porous structure of nanoporous materials.<sup>31</sup> The PSDs obtained from the NLDFT model (Fig. S10†) confirm that porous/wrinkled RGO has micropores and a higher number of mesopores than stacked RGO. In addition, the higher degree of mesoporosity of porous/wrinkled RGO is supported by the specific surface area data in Table S1.† Note that the pore volume increased for porous/wrinkled RGO in comparison to stacked RGO (Table S1†), indicating that swelling/shrinking treatment may in fact be contributing to the observed wrinkling, and thus playing a central role in micro/mesoporosity of porous/wrinkled RGO. As shown in the PSDs (Fig. S10†), stacked RGO shows a sharp peak at 3.9 nm, while after swelling/shrinking treatment, a new peak appears at ~1.9 nm for porous/wrinkled RGO. The full-width at half-maximum (FWHM) of the peak at 3.9 nm increases due to the peak shoulder at 2.9 nm, suggesting that the mesopores formed by the big ripples on stacked RGO were shifted to smaller wrinkles or smaller micro/mesopores. The mesopores may be generated in the process of thermal treatment of

wrinkled GO@shrunken PS by the spaces between RGO nanosheets<sup>8</sup> and wrinkled GO walls of the macropores. The hierarchical porous/wrinkled RGO with macro/mesoporous channels is favorable for fast Li-ion diffusion from different orientations, and is more accessible to Li-ion intercalation/embedding sites created by open pores and wrinkles. From Fig. 4, we conclude the synthesized wrinkled GO@shrunken PS material has the ability to generate 3D hierarchical architectures that could serve as excellent anode materials in LIBs after the removal of the core PS.

### 3.4. Electrochemical properties of porous/wrinkled RGO anode

Fig. 5a shows cyclic voltammetry (CV) curves of porous/wrinkled RGO between 0.002 and 3.000 V at a scanning rate of 0.1 mV s<sup>-1</sup>. The first cycle reduction peak is located at very low potential ~0.1 V. In subsequent cycles, CV profiles were almost identical, which demonstrates structural integrity of the porous/wrinkled RGO electrodes is well maintained during charge–discharge cycles.<sup>32</sup> Fig. 5b shows typical discharge/charge voltage profiles of porous/wrinkled RGO anodes at the 0.2C rate (1C = 372 mA g<sup>-1</sup>) between 0.002 V and 3.000 V. For the initial discharge curve, a rapid potential drop is observed and a sloping plateau appears around 0.6 V. The second to fourth discharge–charge curves lack obvious plateaus, which corresponds to various intercalation compounds such as Li<sub>7</sub>C<sub>14</sub> to Li<sub>18</sub>C<sub>24</sub>, rather than the commonly reported LiC<sub>6</sub> for graphite electrodes.<sup>32</sup> It has been demonstrated that more Li-ions can access defect sites of graphene during cycling;<sup>33</sup> the presence of significant amounts of N-doped defect sites in our synthesized porous/wrinkled RGO anodes is expected to enhance Li intercalation.

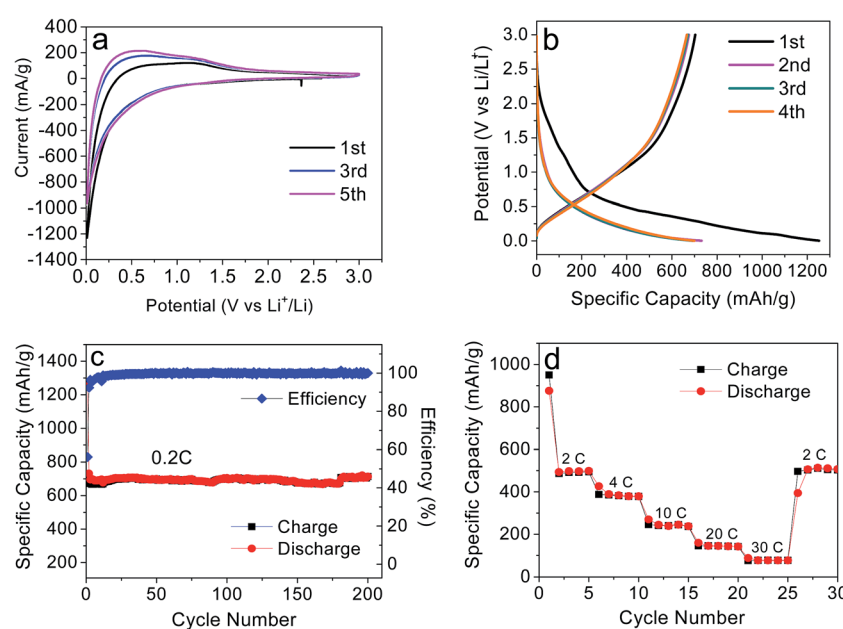


Fig. 5 (a) Cyclic voltammograms (CV) of porous/wrinkled RGO. (b) Galvanostatic charge–discharge profiles of porous/wrinkled RGO at a current rate of 0.2C. (c) Cycle performance and coulombic efficiency of porous/wrinkled RGO at a current rate of 0.2C. (d) Rate capability of porous/wrinkled RGO cycled at different current rates (2C, 4C, 10C, 20C, 30C, and 2C).

Cycling performance of the porous/wrinkled RGO anodes, measured at 0.2C for 200 cycles, is shown in Fig. 5c. The first discharge and charge capacities were 1240 and 750 mA h g<sup>-1</sup>, respectively. After 200 cycles, the reversible capacity was stabilized at approximately 720 mA h g<sup>-1</sup>, delivering almost 100% coulombic efficiency. The high capacity of the porous/wrinkled RGO is attributed to curled walls and macro/mesopores of RGO structure. A previous study<sup>34</sup> suggested the capacity exhibited below 0.5 V (vs. Li/Li<sup>+</sup>) is from Li intercalation into the graphene layers, while the capacity above 0.5 V is ascribed to the faradic capacitance on the surface or on the edge sites of RGO sheets. Moreover, porous/wrinkled RGO exhibited impressive rate performance (Fig. 5d).<sup>21,22,32-34</sup> Even at very high discharge-charge rates (20C and 30C), the anode still delivered ~160 and ~80 mA h g<sup>-1</sup>, respectively. In particular, when the current rate was decreased back to its initial value of 2C after a total of 25 cycles, the reversible capacity was still retained at 490 mA h g<sup>-1</sup>. Successful fabrication of porous/wrinkled RGO for LIB anodes *via* microgel-assisted assembly is evident from the excellent electrochemical behavior as shown in Fig. 5.

To highlight the superiority of our unique porous/wrinkled RGO materials, we tested the samples at a current rate of 4C. For comparison, stacked RGO anodes were also investigated under the same conditions and results are presented in Fig. 6a. Apparently, a porous/wrinkled RGO anode demonstrates a noticeably higher reversible capacity than a stacked RGO anode, with a stable reversible capacity of 400 mA h g<sup>-1</sup> even after 200 cycles. As expected, the porous/wrinkled RGO anode exhibits an extremely durable rate capability, as displayed in Fig. 6b. In contrast, the stacked RGO anode shows a significantly lower rate capability (Fig. 6b). The electrode performance observed in Fig. 6 is consistent with the N<sub>2</sub> physisorption data in Fig. 4d and S9† which shows a lower surface area for stacked RGO in comparison to porous/wrinkled RGO. The low surface area of stacked RGO is expected to result in a decrease in the number of sites for Li-ion insertion and as a consequence, a lower reversible capacity than that of porous/wrinkled RGO. In addition, it is worthy to point out that the PSDs of stacked RGO and porous/wrinkled RGO (Fig. S9†), modeled by the BJH method, are in the same mesopore range and centered around 3.9 nm even though, as revealed by SEM images in Fig. 4, the former lacks macropores and a wrinkled structure. We

emphasize the mesopores in stacked RGO exist mainly in the interlayer space formed between RGO sheets in the dense RGO layered structure, and, as revealed by the cycling data in Fig. 6, do not facilitate high rate capability. On the other hand, in addition to abundant mesopores including smaller pores centered ~2.0 nm (Fig. S9†), presence of abundant macropores in the porous/wrinkled RGO anode has the benefit of facilitating diffusion of electrolyte and Li-ions from macropores to their connected mesopores with shorter transport distance in comparison to a stacked RGO anode.

As shown in Table 1, the Li storage capacity of our hierarchical porous/wrinkled RGO is higher than most of the reported high-performance pristine and N-doped RGO anodes with different architectures and shapes.<sup>8,13,27,35-49</sup> The reversible capacity at low (0.2C)-to-high (20C) charge-discharge rates for our porous/wrinkled RGO sample falls at the top of all RGO anodes with only N, S-co-doped graphene, and CVD-grown graphene exhibiting superior performance. The superior performance of N, S-co-doped graphene may be due to the combined doping of RGO with N and S, which is associated with improved electronic conductivity and Li electroactivity.<sup>35,39,46,50</sup> It is possible the Li storage capacity of our electrode can be improved further by increasing the dopant concentration. Our microgel-assisted process has advantages over conventional methods listed in Table 1. Chemical composition of our PS template is highly flexible as it is synthesized *via* co-polymerization of various functional monomers, thus allowing for introduction of different dopants; for example, the pyridine monomer used in this study is a good source for high-concentration doping of N. Although CVD-grown graphene shows superior performance,<sup>11</sup> we emphasize that unlike the CVD process, the microgel-assisted assembly process has a higher practical application potential due to the advantages of simplicity, scalability, and low cost.

We attribute the improved performance of our porous/wrinkled RGO anode to the mesoporous structure generated by the highly wrinkled RGO and the macropores created after removal of the PS template. In particular, the wrinkled RGO structure provides a high surface area that facilitates rapid charge transfer and minimizes polarization effects. In addition, the macroporous structure is favorable for efficient diffusion of Li ions into deep sites in the bulk RGO. An important distinguishing feature of our wrinkled RGO is that the macropore and highly

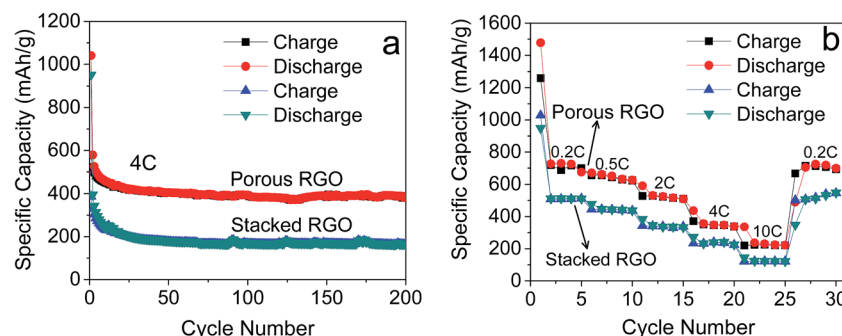


Fig. 6 (a) Comparison of cycle performance of porous/wrinkled RGO and stacked RGO cycled at a current rate of 4C. (b) Comparison of rate capability of porous/wrinkled RGO and stacked RGO cycled at different current rates (0.2C, 0.5C, 2C, 4C, 10C, and 0.2C).

**Table 1** Comparison of electrode performance of porous/wrinkled RGO synthesized using a microgel-assisted method and a variety of high-performance carbon, graphene and RGO anodes in the literature

| Shape     | Materials/architecture            | Preparation method                              | Current C-rate (l/h)/capacities (mA h g <sup>-1</sup> ) |          |           |           |         | Surface area (m <sup>2</sup> g <sup>-1</sup> )           | Ref. |
|-----------|-----------------------------------|---|---|----------|-----------|-----------|---------|--|------|
| Sphere    | RGO hollow sphere/wrinkled wall   | Swelling & shrinking of PS                      | 0.2/720   | 2/510    | 10/260    | 20/160    | 276     | Our work<br>8<br>13<br>38<br>39<br>46<br>48              |      |
|           | RGO hollow sphere/ultrathin shell | SiO <sub>2</sub> template                       | 0.27/650  | 1.34/434 | 8.07/287  | 13.44/249 | 248.3   |  |      |
|           | C hollow sphere/mesoporous wall   | SiO <sub>2</sub> template                       | 0.2/600   | 1/390    | 5/270     | 10/200    | 970     |  |      |
|           | C sphere@carbon black/core-shell  | Spray drying                                    | 0.13/450  | 0.27/410 | 1.34/350  | 2.7/300   | 49      |  |      |
|           | N-riched C sphere                 | SiO <sub>2</sub> template & N doping            | 1.34/542  | 2.7/410  | 5.4/293   | 8.07/215  | 67.4    |  |      |
|           | N, S co-doped RGO hollow sphere   | Nickel foam & sulfonated PS                     | 1.34/610  | 2.7/590  | 5.4/440   | 26.9/380  | 70      |  |      |
|           | C hollow sphere/mesoporous wall   | SiO <sub>2</sub> template & CVD growth          | 0.2/268   | 0.5/255  | 1/189     | 10/125    | 771     |  |      |
|           | Highly porous graphene            | CVD growth                                      | 1/707   | 2/650    | 5/544     | 20/203    | 1654    |  |      |
| Sheet     | Graphitic C                       | NaCl template                                   | 1/530   | 2/500    | 10/380    | 30/115    | 469.5   | 10<br>51<br>27<br>37<br>40<br>41<br>42<br>43<br>44<br>47 |      |
|           | N-doped graphene                  | Pyrolysis & MgO template                        | 0.27/655  | 1.34/300 | 2.7/259   | 13.44/150 | 466     |  |      |
|           | Free standing RGO                 | Freeze-drying                                   | 0.54/600  | 1.34/540 | 2.7/500   | 5.4/450   | 148     |  |      |
|           | Sandwiched RGO@N-doped C          | Pyrolysis                                       | 0.54/638  | 1.34/511 | 5.4/286   | 26.9/98   | 327     |  |      |
|           | Folded RGO                        | Freeze-drying & thermal reduction               | 0.54/557  | 1.34/268 | 2.7/169   | 4.03/141  | —       |  |      |
|           | Free standing holey RGO           | Mechanical cavitation-chemical oxidation        | 0.27/320  | 0.67/287 | 2.7/200   | 5.4/175   | 15      |  |      |
|           | Mesoporous graphene/9 nm pores    | Monomicelle close-packing assembly              | 0.27/770  | 0.54/540 | 1.34/430  | 13.44/255 | 281     |  |      |
|           | C fibres grown on graphene        | CVD growth                                      | 0.2/420   | 1/329    | 5/200     | 10/189    | 315     |  |      |
|           | Free standing RGO                 | Photothermal reduction                          | 1/545   | 5/375    | 20/240    | —         | 200–300 |  |      |
|           | Sandwiched RGO@mesoporous C       | Self-assembly                                   | 0.2/770   | 1/540    | 5/370     | 20/250    | 910     |  |      |
| Gel Cloth | RGO@melamine-formaldehyde         | Freeze-drying                                   | 0.27/672  | 0.54/560 | 1.1/460   | 4.03/317  | 1170    | 36   |      |
|           | N-doped C                         | Cotton cloth template & CVD growth              | 2.7/500   | 5.4/369  | 13.44/183 | 26.9/110  | 1890    | 35   |      |
| Sponge    | Meso & macroporous C              | Polystyrene template <i>via</i> mesophase pitch | 0.2/470   | 1/320    | 5/200     | —         | 170     | 45   |      |

wrinkled RGO sheet properties can be easily tuned *via* changing the size of core PS. Further, the void that exists between neighboring wrinkles of RGO could offer a safe region for depositing active electrode materials (metal or metal oxide) and accommodating the large volume changes that typically occur during cycling.

## 4. Conclusions

Hierarchical porous/wrinkled RGO anodes were successfully synthesized utilizing a unique approach involving swelling and shrinking of a polymer template. Selection of solvents plays a critical role in the synthesis of the 3D hierarchical porous RGO. The GO@microgel was first obtained in the “good solvent” (NMP) and then shrunk in a “poor solvent” (water) to obtain wrinkled GO@shrunken PS. During the shrinking process, the outer surface of GO was wrinkled and roughened, resulting in formation of mesochannels on the wrinkled GO@shrunken PS surfaces. The resulting macro/mesoporous and wrinkled RGO anode materials, obtained after annealing of the polymer spheres provided favorable transport kinetics for both Li ions and electrons. As a result, high

reversible capacity and durability (720 mA h g<sup>-1</sup> at 0.2C current rate after 200 cycles), and high rate capability (~160 mA h g<sup>-1</sup> at 20C) were achieved as electrodes of Li-ion cells. Reversible capacity at low (0.2C)-to-high (20C) charge-discharge rates for our porous/wrinkled RGO sample falls at the top of all RGO anodes. Consequently, it is reasonable to conclude the microgel-assisted method demonstrated in this study has the potential of enabling future design of graphene-based electrodes for various energy storage devices.

## Conflicts of interest

There are no conflicts to declare.

## Acknowledgements

Financial support from Kansas State University (start-up funds) and the National Science Foundation under Award Number EPS-0903806 and matching support from the state of Kansas through the Kansas Board of Regents are gratefully

acknowledged. The authors are grateful to Prof. Keith Hohn and Zahraa Alauda for XPS characterization.

## References

- 1 M. Yoshio, R. J. Brodd and A. Kozawa, *L.-I. Batteries*, 2009.
- 2 B. Scrosati, J. Hassoun and Y.-K. Sun, *Energy Environ. Sci.*, 2011, **4**, 3287–3295.
- 3 H. Wang, X. Li, M. Baker-Fales and P. B. Amama, *Curr. Opin. Chem. Eng.*, 2016, **13**, 124–132.
- 4 H. Wang, J. Xie, M. Follette, T. C. Back and P. B. Amama, *RSC Adv.*, 2016, **6**, 83117–83125.
- 5 E. Yoo, J. Kim, E. Hosono, H.-s. Zhou, T. Kudo and I. Honma, *Nano Lett.*, 2008, **8**, 2277–2282.
- 6 Y. Zhu, S. Murali, W. Cai, X. Li, J. W. Suk, J. R. Potts and R. S. Ruoff, *Adv. Mater.*, 2010, **22**, 3906–3924.
- 7 S. Park and R. S. Ruoff, *Nat. Nanotechnol.*, 2009, **4**, 217–224.
- 8 D. Cai, L. Ding, S. Wang, Z. Li, M. Zhu and H. Wang, *Electrochim. Acta*, 2014, **139**, 96–103.
- 9 B. G. Choi, M. Yang, W. H. Hong, J. W. Choi and Y. S. Huh, *ACS Nano*, 2012, **6**, 4020–4028.
- 10 S.-H. Park, H.-K. Kim, S.-B. Yoon, C.-W. Lee, D. Ahn, S.-I. Lee, K. C. Roh and K.-B. Kim, *Chem. Mater.*, 2015, **27**, 457–465.
- 11 Z. Fan, J. Yan, G. Ning, T. Wei, L. Zhi and F. Wei, *Carbon*, 2013, **60**, 558–561.
- 12 J. L. Vickery, A. J. Patil and S. Mann, *Adv. Mater.*, 2009, **21**, 2180–2184.
- 13 S. Yang, X. Feng, L. Zhi, Q. Cao, J. Maier and K. Müllen, *Adv. Mater.*, 2010, **22**, 838–842.
- 14 S. Yin, Y. Zhang, J. Kong, C. Zou, C. M. Li, X. Lu, J. Ma, F. Y. C. Boey and X. Chen, *ACS Nano*, 2011, **5**, 3831–3838.
- 15 S. Stankovich, D. A. Dikin, G. H. Domke, K. M. Kohlhaas, E. J. Zimney, E. A. Stach, R. D. Piner, S. T. Nguyen and R. S. Ruoff, *Nature*, 2006, **442**, 282–286.
- 16 A. Singhal, K. Dubey, Y. Bhardwaj, D. Jain, S. Choudhury and A. Tyagi, *RSC Adv.*, 2013, **3**, 20913–20921.
- 17 Z. Guo, L. L. Henry, V. Palshin and E. J. Podlaha, *J. Mater. Chem.*, 2006, **16**, 1772–1777.
- 18 S. M. Safiullah, K. A. Wasi and K. A. Basha, *Polymer*, 2015, **66**, 29–37.
- 19 S. Tolue, M. R. Moghbeli and S. M. Ghafelebashi, *Eur. Polym. J.*, 2009, **45**, 714–720.
- 20 Y. Dai, H. Pang, J. Huang, Y. Yang, H. Huang, K. Wang, Z. Ma and B. Liao, *RSC Adv.*, 2016, **6**, 34514–34520.
- 21 F. H. B. Baldovino, A. T. Quirain, N. P. Dugos, S. A. Roces, M. Koinuma, M. Yuasa and T. Kida, *RSC Adv.*, 2017, **7**, 3852.
- 22 W. Xiao, P. Zhao, S. Deng and N. Zhang, *New J. Chem.*, 2015, **39**, 3719–3727.
- 23 W. Li, X.-Z. Tang, H.-B. Zhang, Z.-G. Jiang, Z.-Z. Yu, X.-S. Du and Y.-W. Mai, *Carbon*, 2011, **49**, 4724–4730.
- 24 S. Chakraborty, S. Saha, V. R. Dhanak, K. Biswas, M. Barbezat, G. P. Terrasi and A. K. Chakraborty, *RSC Adv.*, 2016, **6**, 67916–67924.
- 25 C. Petit, *Factors Affecting the Removal of Ammonia from Air on Carbonaceous Materials*, Springer, 2012.
- 26 C. Zheng, X. Zhou, H. Cao, G. Wang and Z. Liu, *RSC Adv.*, 2015, **5**, 10739–10745.
- 27 Z. Xing, *et al.*, *Sci. Rep.*, 2016, **6**, 26146.
- 28 P. I. Ravikovich, S. C. O. Domhnall, A. V. Neimark, F. Schueth and K. K. Unger, *Langmuir*, 1995, **11**, 4765–4772.
- 29 M. W. Maddox, J. P. Olivier and K. E. Gubbins, *Langmuir*, 1997, **13**, 1737–1745.
- 30 P. I. Ravikovich, D. Wei, W. T. Chueh, G. L. Haller and A. V. Neimark, *J. Phys. Chem. B*, 1997, **101**, 3671–3679.
- 31 A. V. Neimark, *Langmuir*, 1995, **11**, 4183–4184.
- 32 F. Xiang, R. Mukherjee, J. Zhong, Y. Xia, N. Gu, Z. Yang and N. Koratkar, *Energy Storage Materials*, 2015, **1**, 9–16.
- 33 F. Xiang, J. Zhong, N. Gu, R. Mukherjee, I.-K. Oh, N. Koratkar and Z. Yang, *Carbon*, 2014, **75**, 201–208.
- 34 T. Hu, X. Sun, H. Sun, G. Xin, D. Shao, C. Liu and J. Lian, *Phys. Chem. Chem. Phys.*, 2014, **16**, 1060–1066.
- 35 H. Bi, Z. Liu, F. Xu, Y. Tang, T. Lin and F. Huang, *J. Mater. Chem. A*, 2016, **4**, 11762–11767.
- 36 Z.-Y. Sui, C. Wang, Q.-S. Yang, K. Shu, Y.-W. Liu, B.-H. Han and G. G. Wallace, *J. Mater. Chem. A*, 2015, **3**, 18229–18237.
- 37 K. Shu, C. Wang, S. Li, C. Zhao, Y. Yang, H. Liu and G. Wallace, *J. Mater. Chem. A*, 2015, **3**, 4428–4434.
- 38 L. Zhang, M. Zhang, Y. Wang, Z. Zhang, G. Kan, C. Wang, Z. Zhong and F. Su, *J. Mater. Chem. A*, 2014, **2**, 10161–10168.
- 39 D. Li, L.-X. Ding, H. Chen, S. Wang, Z. Li, M. Zhu and H. Wang, *J. Mater. Chem. A*, 2014, **2**, 16617–16622.
- 40 X. Liu, J. Zhang, S. Guo and N. Pinna, *J. Mater. Chem. A*, 2016, **4**, 1423–1431.
- 41 F. Liu, S. Song, D. Xue and H. Zhang, *Adv. Mater.*, 2012, **24**, 1089–1094.
- 42 X. Zhao, C. M. Hayner, M. C. Kung and H. H. Kung, *ACS Nano*, 2011, **5**, 8739–8749.
- 43 Y. Fang, Y. Lv, R. Che, H. Wu, X. Zhang, D. Gu, G. Zheng and D. Zhao, *J. Am. Chem. Soc.*, 2013, **135**, 1524–1530.
- 44 Z.-J. Fan, J. Yan, T. Wei, G.-Q. Ning, L.-J. Zhi, J.-C. Liu, D.-X. Cao, G.-L. Wang and F. Wei, *ACS Nano*, 2011, **5**, 2787–2794.
- 45 P. Adelhelm, Y. S. Hu, L. Chuenchom, M. Antonietti, B. M. Smarsly and J. Maier, *Adv. Mater.*, 2007, **19**, 4012–4017.
- 46 Z.-L. Wang, D. Xu, H.-G. Wang, Z. Wu and X.-B. Zhang, *ACS Nano*, 2013, **7**, 2422–2430.
- 47 R. Mukherjee, A. V. Thomas, A. Krishnamurthy and N. Koratkar, *ACS Nano*, 2012, **6**, 7867–7878.
- 48 X. Chen, K. Kierzek, Z. Jiang, H. Chen, T. Tang, M. Wojtoniszak, R. J. Kalenczuk, P. K. Chu and E. Borowiak-Palen, *J. Phys. Chem. C*, 2011, **115**, 17717–17724.
- 49 S. Yang, X. Feng, L. Wang, K. Tang, J. Maier and K. Müllen, *Angew. Chem., Int. Ed.*, 2010, **49**, 4795–4799.
- 50 Y. Yan, Y.-X. Yin, S. Xin, Y.-G. Guo and L.-J. Wan, *Chem. Commun.*, 2012, **48**, 10663–10665.
- 51 L. Chen, Z. Wang, C. He, N. Zhao, C. Shi, E. Liu and J. Li, *ACS Appl. Mater. Interfaces*, 2013, **5**, 9537–9545.